

1 **Facile synthesis of high-performance indium nanocrystals for**
2 **selective CO₂-to-formate electroreduction**

3 Liangping Xiao^a, Xiao Liu^a, Renwu Zhou^b, Tianqi Zhang^b, Rusen Zhou^{a,b,c,*}, Bo Ouyang^{d,*},
4 Erjun Kan^d, Patrick J. Cullen^b, Kostya (Ken) Ostrikov^c, Xin Tu^{e,*}

5 ^a *State Key Laboratory of Physical Chemistry of Solid Surfaces, Department of Chemistry,*
6 *College of Chemistry and Chemical Engineering, Xiamen University, Xiamen 361005, China*

7 ^b *School of Chemical and Biomolecular Engineering, University of Sydney, NSW 2008,*
8 *Australia*

9 ^c *School of Chemistry and Physics, Queensland University of Technology, Brisbane,*
10 *QLD4000, Australia*

11 ^d *Department of Applied Physics & Institution of Energy & Microstructure, Nanjing*
12 *University of Science & Technology, Nanjing, China*

13 ^e *Department of Electrical Engineering and Electronics, University of Liverpool, Liverpool,*
14 *L69 3GJ, United Kingdom*

15 *Corresponding authors:

16 zhourusen2008@gmail.com (R. Zhou); ouyangboyi@njust.edu.cn (B. Ouyang);

17 xin.tu@liverpool.ac.uk (X. Tu)

18

19

20

21

22

23 **Abstract**

24 Selective electrocatalytic reduction of CO₂ to formate has received increasing interest for CO₂
25 conversion and utilization. Yet, the CO₂ reduction process still faces major challenges, partly
26 due to the lack of cost-effective, highly active, selective and stable electrocatalysts. Here, we
27 report a mesoporous indium (*mp*-In) electrocatalyst composed of nanobelts synthesized *via* a
28 simple solution-based approach for selective CO₂ reduction to formate. The *mp*-In nanocrystals
29 provide enlarged surface areas, abundant surface active sites, and edge/low-coordinated sites.
30 Such advantages afford the *mp*-In with an outstanding electrocatalytic performance for the
31 CO₂-to-formate conversion. A high formate selectivity, with a Faradaic efficiency (FE) of >
32 90% was achieved over a potential of -0.95 V to -1.1 V (*vs* V_{RHE}). The *mp*-In catalyst showed
33 excellent durability, reflected by the stable formate selectivity and current density over a 24 h
34 reaction period. Density functional theory (DFT) calculations reveal that the stabilization of
35 the intermediate OCHO* on the In-plane surfaces is energetically feasible, further elucidating
36 the origin of its enhanced CO₂-to-formate activity and selectivity. This work may offer valuable
37 insights for the facile fabrication of porous hierarchical nanostructures for electrocatalytic and
38 selective reduction of CO₂.

39

40 **Keywords:** CO₂ reduction; Electrocatalysis; Mesoporous indium catalysts; Formate; CO₂
41 conversion

42

43

44

45 **1. Introduction**

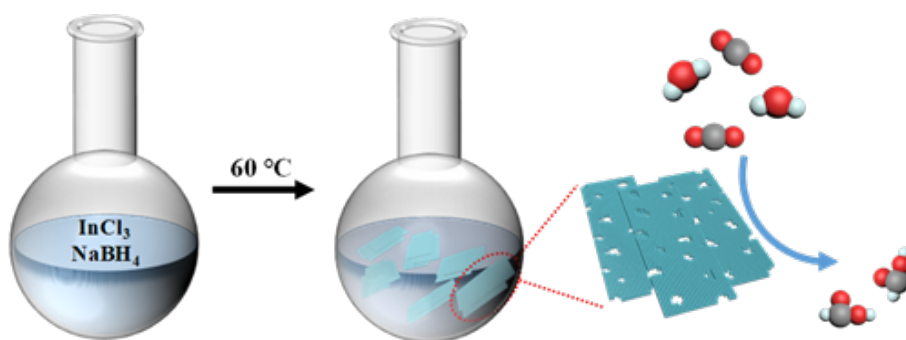
46 Electrochemical reduction of CO₂ provides an attractive strategy to harvest green fuels and
47 chemicals from CO₂ emissions, and importantly help mitigate global warming and climate
48 change [1-4]. Considering its efficiency, controllability at moderate conditions and feasibility
49 for coupling with renewable energy, particularly intermittent renewable electricity, this process
50 has great potential to support the transition to a low carbon circular economy [5-7]. Formate
51 (HCOO⁻) or formic acid (HCOOH) is a widely explored hydrogen storage carrier, a commonly
52 used chemical intermediate for industrial production, and a potential chemical fuel for the
53 direct formic acid fuel cells [8,9]. It is one of the most favorable products in the electrocatalytic
54 CO₂ reduction reaction (CO₂RR) as the CO₂-to-formate conversion has a low equilibrium
55 potential (CO₂ → HCOOH, 0 V at pH = 7), and requires only two electrons, leading to the
56 most economical viability based on a recent techno-economic analysis [10]. In addition,
57 compared to other products in CO₂RR, higher selectivities of formate are generally achieved,
58 since the adsorption of the key intermediates (*OCHO and *COOH) on the catalyst surfaces is
59 usually endothermic [11]. Yet, there are still several inherent challenges in the electrocatalytic
60 CO₂RR to formate because of the high thermodynamic stability of CO₂ and the multiple-steps
61 involved in the reaction [12]. Additionally, the close distribution of the warranted
62 thermodynamic energy for the competing reactions, in particular, the hydrogen evolution
63 reaction (HER), further reduces the efficiency and selectivity of CO₂RR [13]. Consequently, it
64 is important to develop high-performance catalysts with high conversion efficiency, persistent
65 activity, and stability for selective CO₂-to-formate electroreduction.

66 Metals, mainly located in the groups of IB [14-17], III to V A in the periodic table, have

67 so far been trialed as potential electrocatalyst candidates for the conversion of CO₂ to formate
68 [18-21]. However, many of these are costly, toxic (e.g., Cd, Hg, Ti and Pb) [22-24], and/or have
69 low selectivity (e.g., Sn-based materials) [25-27], limiting the use of such metal-based catalysts
70 at a commercial scale. Indium (In) has also been suggested for its CO₂-to-formate activity and
71 promoted for its advantages emerged among its neighbors due to its superiorities from the
72 viewpoint of low toxicity and environmental friendliness [28-30]. A Faradaic efficiency (FE)
73 of over 80% in aqueous electrolytes is generally obtained for different In-based electrocatalysts
74 [31-34]. However, many of the In-based catalysts still suffer from low current densities (e.g.,
75 <10 mA cm⁻², even at high potentials) and poor catalyst durability [31,32]. For example, the
76 reported highest current densities for a dendrite In electrode and a gas diffusion In/carbon
77 electrode were only 5.8 and 6.2 mA cm⁻², respectively [33,34]. These In-based catalysts have
78 large sizes and small specific surface areas; this results in the lack of sufficient active sites,
79 which may directly lead to their poor electrocatalytic performance. Recent studies have
80 suggested that manipulating or engineering the nanostructures of the electrode materials is an
81 effective approach to fabricate electrocatalysts with developed porous structures [30,10,35].
82 The enlarged surface areas and enriched surface active sites associated with such porous
83 nanostructures could enhance the catalytic activities. A remarkably high current density of over
84 60 mA cm⁻² together with a high formate FE (~90%) was reported when using a 3D hierarchical
85 porous indium electrocatalyst for CO₂RR [10]. However, the engineering of indium
86 nanostructures remains challenging due to the special physicochemical properties of indium.
87 For instance, in the aforementioned study, an electrochemical deposition method is required
88 for the fabrication of porous In. Such a method may limit the production rate and the feasibility

89 of catalyst mass-production.

90 Herein, we report a mesoporous hierarchical In (*mp*-In) nanocrystal composed of
91 nanobelts, which was synthesized *via* a facile and greener method (**Figure 1**) without using
92 any extra templates. The hydrogen bubbles generated from the hydrolysis of NaBH₄ serve as
93 the geometric templates [36]. The solution-based fabrication method enables the designed
94 catalyst to possess a stable nanostructure with a high surface area and abundant active and edge
95 sites. The catalytic activity for CO₂-to-formate electroreduction over a broad potential range
96 (*vs* reversible hydrogen electrode (RHE), V_{RHE}) of the as-prepared *mp*-In catalyst was
97 demonstrated (FE and current density for formate production, and stability) and compared to
98 other reported In-based catalysts. In addition, the selective nature for formate formation was
99 further revealed by density functional theory (DFT) calculations to elucidate the plane-
100 dependent catalytic activity of In [10,37]. We expect the results from this study will provide a
101 promising high-performing CO₂-to-formate electrocatalyst and valuable insights into the facile
102 fabrication of porous hierarchical nanostructures for selective CO₂RR.



103

104 **Figure 1** The synthesis of the mesoporous In (*mp*-In) nanocrystals *via* a facile solution method

105 at 60 °C with NaBH₄ as the reductant.

106

107 **2. Experimental section**

108 **2.1 Materials**

109 InCl_3 (99.999% metal basis), NaBH_4 and Nafion N-117 membrane with a thickness of
110 0.18 mm were purchased from Alfa Aesar. KHCO_3 was purchased from Sigma Aldrich and the
111 commercial indium powder from Aladdin. All chemicals were used directly without extra
112 purification. Milli-Q water (Millipore, 18.2 $\text{M}\Omega$ cm) was used to prepare the electrolyte
113 solutions. Hydrogen (H_2 , 99.99%), argon (Ar, 99.999%), compressed air (extra dry) and carbon
114 dioxide (CO_2 , 99.99%) were purchased from Linde Group.

115

116 **2.2 Material synthesis and characterization**

117 Before synthesis, transparent solutions of InCl_3 (132.7 mg dissolved in 20 mL H_2O) and
118 NaBH_4 (22.7 mg in 20 mL H_2O) were prepared, respectively. The InCl_3 solution was then
119 heated to 60 °C, prior to mixing with the NaBH_4 solution. The mixture refluxes were vigorously
120 stirred at atmospheric pressure for around 10 min. Finally, the obtained silver-gray precipitates
121 were washed with deionized water by centrifugation before oven-drying and then termed
122 mesoporous hierarchical In (*mp*-In). To understand the contribution of NaBH_4 on tuning the
123 porous structure of the In particles, sodium citrate (208.9 mg dissolved in 20 mL H_2O) was
124 used to replace the NaBH_4 , with the prepared In catalyst termed as *nano*-In.

125 Transmission electron microscope (TEM) images were taken using an FEI F20 with an
126 acceleration voltage of 200 kV. High-resolution TEM (HRTEM) images, high angle annular
127 dark-field scanning transmission electron microscopy (HAADF-STEM), elemental mapping
128 and the energy-dispersive X-ray spectroscopy (EDS) patterns were collected from an FEI

129 Tecnai Talos operated at 200 kV. X-ray photoelectron spectroscopy (XPS, PHI Quantum 2000)
130 with an X-ray source of Mg S-6 K α was used to study the chemical composition of the In
131 catalysts. Software XPS peak41 was used to deconvolute the curves and fit the results. X-ray
132 diffraction (XRD) patterns of the catalysts were obtained using a Bruker-axs (Cu K α X-ray
133 source, 40 kV and 40 mA). The N₂ adsorption-desorption analysis was performed using a
134 TriStar II Plus to obtain the surface areas and pore distributions of the catalysts. The amount of
135 adsorbed CO₂ was measured using a TriStar II physisorption analyzer. *In situ* diffuse Fourier
136 transform infrared spectroscopy (DRIFTS) was conducted using a VERTEX 70 FTIR (Bruker).
137 CO₂ gas was pumped into the sample at a flow rate of 20 mL min⁻¹, and Ar was injected after
138 10 min. After 10 min, the peak of CO₂ was detected.

139

140 **2.3 Electrochemical measurements**

141 An electrochemical workstation (CHI660C) with a gas-tight H-type electrochemical cell
142 separated with a Nafion-117 membrane was used for the electrochemical measurements. 1 mg
143 of In (*mp*-In, *nano*-In or commercial In) was dispersed in 180 μ L of ethanol with the addition
144 of 20 μ L of 5 wt.% Nafion. The mixture was sonicated for 30 min to form a homogenous ink.
145 The ink was drop-cast onto a 1 \times 1 cm² carbon cloth (HCP020P, from HESEN) to obtain a
146 catalyst area loading of 1 mg cm⁻². The carbon cloth was washed with 0.1 mol L⁻¹ HCl and
147 ethanol before being used as the working electrode. A piece of the platinum plate (1 cm \times 1 cm)
148 and a saturated calomel electrode (SCE) were applied as the counter and reference electrodes,
149 respectively. The working and the reference electrodes were placed in the cathodic
150 compartment, while the counter electrode was placed in the anodic compartment. Each

151 compartment of the cell was filled with the KHCO_3 electrolyte (0.1 M, 30 mL, Sigma Aldrich).
152 The electrolyte was pre-saturated with CO_2 . During the measurement, CO_2 was continuously
153 bubbled into the cathode compartment at a flow rate of 20 mL min^{-1} . Cyclic voltammetry (CV)
154 and linear sweep voltammetry (LSV) was carried out at a scan rate of 50 mV s^{-1} . All potentials
155 were converted to the RHE scale ($E_{\text{RHE}} = E_{\text{SCE}} + 0.241 \times V_{\text{Potential}} + 0.0591 \times V_{\text{Potential}} \times \text{pH}$).

156 The electrochemical surface area (ECSA) of the nanocatalysts with similar composition
157 is proportional to the electrochemical double-layer capacitance (C_{dl}) [38]. The C_{dl} was
158 measured by CV in a non-Faradaic region at different scan rates (V_b) of 20, 40, 60, 80, 100,
159 120, 160 and 200 mV s^{-1} in an N_2 -bubbled KHCO_3 (0.1 M, 30 mL), under potentials between
160 -0.6 and -0.4 V . The slopes of those plots of capacitive currents against scan rates reflect the
161 C_{dl} values after being divided by 2. The ECSA can then be calculated from the C_{dl} values based
162 on $\text{ECSA} = C_{\text{dl}}/C_s$. The C_s , defined as the specific capacitance of a flat surface with 1 cm^2 of
163 real surface area, is the C_{dl} of the In foil, with an estimated value of $40 \mu\text{F cm}^{-2}$ for planar metal
164 surfaces [38].

165

166 **2.4 Product analysis**

167 The gas products (H_2 and CO) were analyzed by a gas chromatograph (GC, Agilent 880C)
168 equipped with a thermal conductivity detector (TCD) and a flame ionization detector (FID).
169 The gas products generated in the cathode chamber were automatically injected into the GC
170 (sampling loop) every 7 min for 1 h of reaction. The Faradaic efficiency of gas products was
171 evaluated using the following equations [37, 39]:

$$172 \text{ FE} = \frac{nFVv p_0}{RT_0 I_{\text{total}}} \times 100\% \quad (1)$$

$$173 \quad FE = \frac{2 \times 96485 \left(\frac{C}{mol}\right) \times V \left(\frac{m^3}{s}\right) \times v(vol\%) \times 1.01 \times 10^5 \left(\frac{N}{m^2}\right)}{8.314 \left(\frac{N \cdot m}{mol \cdot K}\right) \times 298(K) \times I_{total} \left(\frac{C}{s}\right)} \times 100\% \quad (2)$$

$$174 \quad FE = \frac{2 \times 96485 \left(\frac{C}{mol}\right) \times V \left(\frac{mL}{min}\right) \times 10^{-6} \left(\frac{m^3}{mL}\right) \times v(vol\%) \times 1.01 \times 10^5 \left(\frac{N}{m^2}\right)}{8.314 \left(\frac{N \cdot m}{mol \cdot K}\right) \times 298(K) \times I_{total} \left(\frac{C}{s}\right) \times 60 \left(\frac{s}{min}\right)} \times 100\% \quad (3)$$

$$175 \quad FE = \frac{0.1315 \times V \left(\frac{mL}{min}\right) \times v(vol\%)}{I_{total}} \times 100\% \quad (4)$$

176 where v is H₂ or CO volume concentration; V is the gas flow rate controlled by a mass flow
 177 controller; I_{total} is the current measured in the constant-potential electrolysis.

178

179 The liquid products were collected after electrolysis and analyzed by ¹H Nuclear magnetic
 180 resonance (NMR) spectroscopy (Agilent 500 MHz) based on the method used in Ref [37]. 500
 181 μL of the catholyte was mixed with 100 μL of D₂O and 0.1 μL of phenol (C₆H₅OH, as the
 182 internal standard). The concentration of formate was quantitatively determined from its NMR
 183 peak area relative to that of the internal standard using the calibration curve from a series of
 184 standard HCOONa solutions (**Figure S1**). **Figure S2** shows the representative ¹H NMR spectra
 185 of the liquid products obtained at different potentials. The FE of HCOOH was calculated using
 186 the following equations:

$$187 \quad FE = \frac{2C_{HCOOH} \times V \times e \times N_A \times 10^{-3}}{Q} \times 100\% \quad (5)$$

$$188 \quad FE = \frac{2C_{HCOOH} \times 30 \text{ mL} \times 1.6 \times 10^{-19} \left(\frac{C}{mol}\right) \times 6.02 \times 10^{23} \times 10^{-3}}{Q} \times 100\% \quad (6)$$

189 where C_{HCOOH} is the concentration of HCOOH in the electrolyte after the electrolysis, and Q is
 190 the total electricity consumed in the electrolysis reaction. The total Faradaic efficiencies for
 191 both gas and liquid products are normalized to 100%.

192

193

194 **2.5 Computational study**

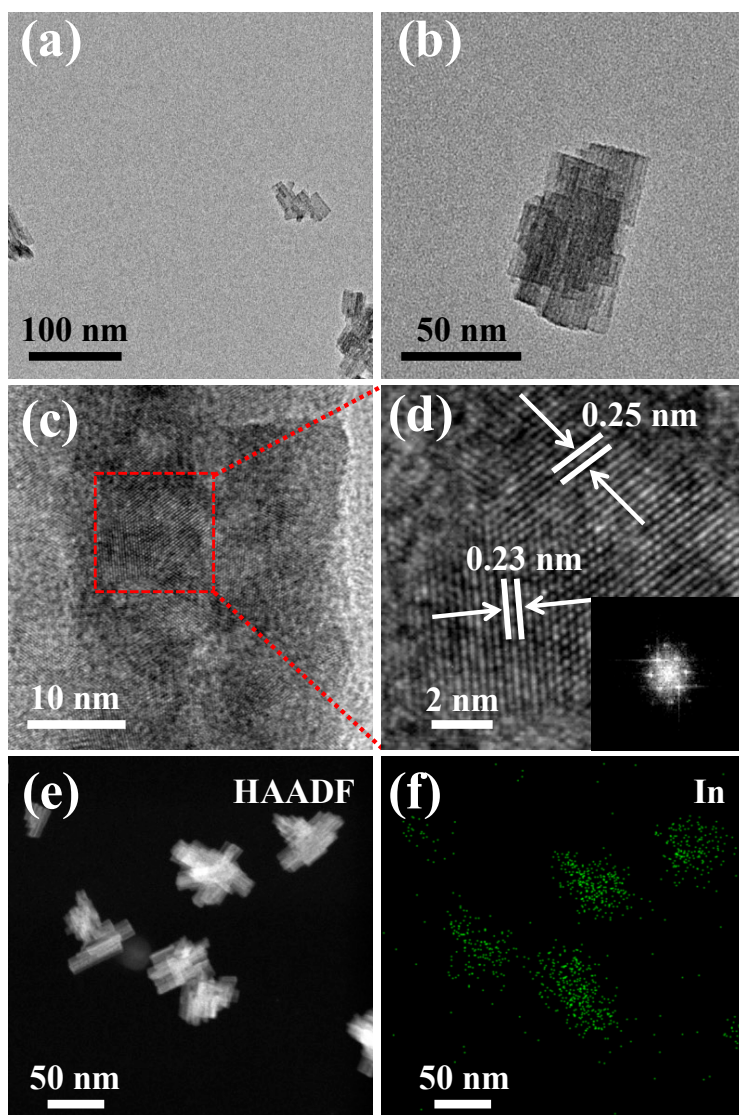
195 The DFT calculations were performed with periodic supercells within the projector
196 augmented wave method implemented in the Vienna Ab Initio Simulation Package (VASP).
197 The Perdew-Burke-Ernzerhof (PBE) formulation of the generalized gradient approximation
198 (GGA) was used to describe the nonlocal exchange and correlation energies. Van der Waals
199 interactions are included in all calculations. The plane-wave basis set with a cut-off energy of
200 500 eV was applied to expand the wave functions, and the convergence criterion for total
201 energy and the force was set to 10^{-6} eV and 0.01 \AA^{-1} . A 20 \AA vacuum layer was added along
202 the normal direction to avoid spurious interactions between the two adjacent images. A K-
203 points sampling of $4 \times 4 \times 1$ was used for all structures. The electrode effect (ΔG_U) and extra pH
204 effect (ΔG_{pH}) were not considered in this work. The adsorption energies for the investigated
205 catalysts were calculated as $E_{\text{ads}} = E_{\text{substrate+adsorbate}} - (E_{\text{substrate}} + E_{\text{adsorbate}})$, where E_{ads} refers to
206 the binding energy between the catalyst and adsorbate; $E_{\text{substrate+adsorbate}}$ stands for the energy of
207 catalyst surface with the adsorbate; $E_{\text{substrate}}$ is the total energy of the catalyst surface without
208 adsorbates; $E_{\text{adsorbate}}$ is the total energy of adsorbate which remains constant in the calculations
209 for different adsorption configurations.

210 The performances were evaluated by calculating the reaction free energy of each step: Δ
211 $G = \Delta E + \Delta \text{EZPE} - T\Delta S$, where the ΔE denotes the adsorption energy, ΔEZPE and ΔS are
212 the changes of zero-point energy and entropy, and the temperature T was set to 300 K.

213

214 **3. Results and discussion**

215 **3.1. Synthesis and characterization of *mp*-In nanocrystals**



216

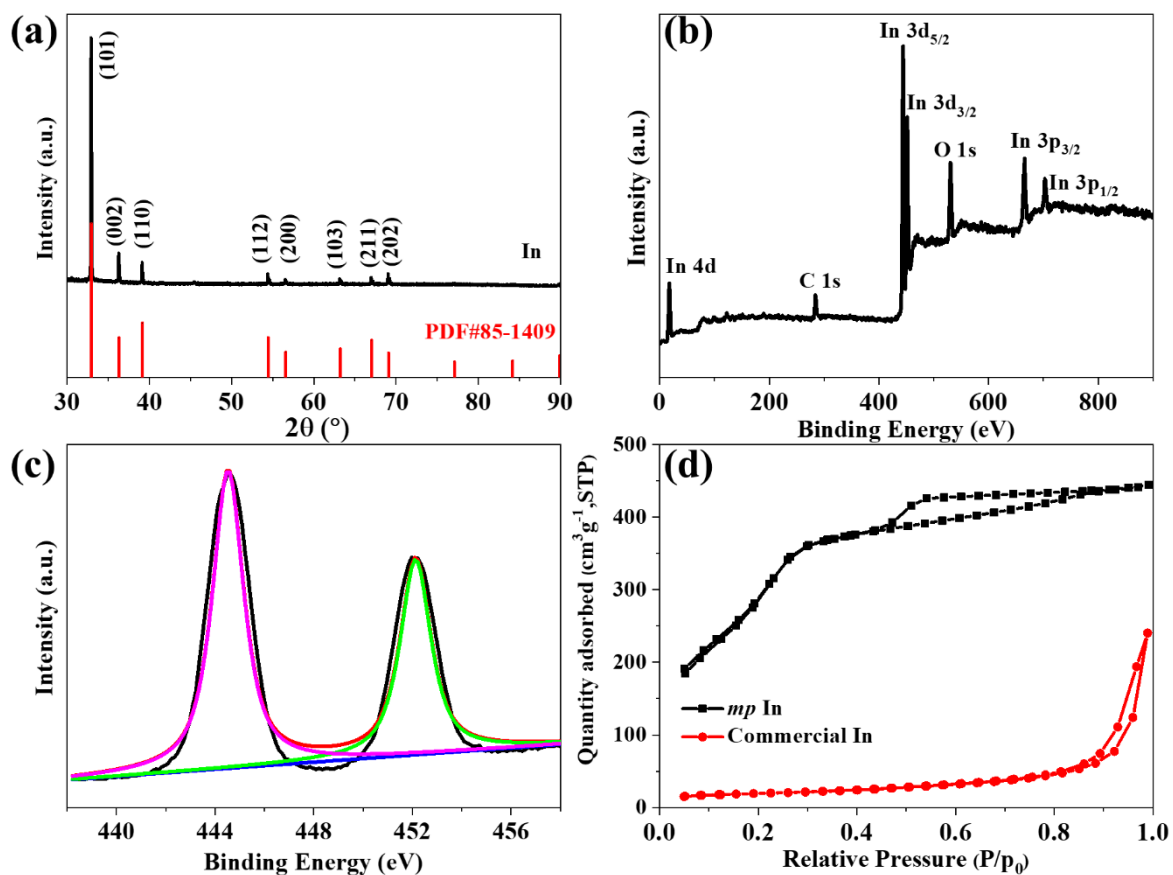
217 **Figure 2** TEM images of the as-synthesized *mp*-In catalyst at (a) low resolution and (b) high
 218 resolution; HRTEM images of the *mp*-In catalyst at (c) low resolution and (d) high resolution
 219 with the FFT image inserted; (e) HAADF-STEM image and (f) the corresponding elemental
 220 mapping of the *mp*-In catalyst.

221 The *mp*-In nanocrystals were prepared by a facile solution method with NaBH₄ as the
 222 reductant at 60 °C. The TEM images show that the *mp*-In nanocrystals are composed of smaller
 223 nanobelts (**Figure 2a**) with an average length of 104.8 ± 15 nm and width of 61.7 ± 10 nm
 224 (**Figure S3a and S3b**). **Figure 2b** and relevant images in and over-focus (**Figure S4**) reveal

225 that the mesoporous structures are uniformly distributed on the surface of the hierarchical *mp*-
226 In catalyst. The hierarchical structure is originated from the stacking of nanobelts, and the
227 dispersed pores and defects at the edges of the nanobelts. As can be seen from the TEM image
228 at low resolution (**Figure S3c**), the *mp*-In nanocrystals have a regular morphology. HRTEM
229 images (**Figures 2c** and **2d**) reveal the lattice fringes with distances of 0.23 nm and 0.25 nm
230 for the *mp*-In catalyst, which correspond to the (110) and (002) planes of the crystal structure
231 of In, respectively. The diffraction pattern in fast Fourier transformation (FFT) (inset of **Figure**
232 **2d**) shows the crystalline nature of In. The *mp*-In nanocrystal was further characterized by
233 HAADF-STEM element mapping, indicating the uniform distribution of In (green) over the
234 whole nanocrystal (**Figure 2e** and **2f**), consistent with the result of the energy-dispersive X-ray
235 spectroscopy (EDS) analysis (**Figure S5**).

236 **Figure 3a** shows the crystalline structures of the as-prepared *mp*-In catalyst. The
237 diffraction peaks at approximately 32.9°, 36.3°, 39.1°, 54.5°, 56.6°, 63.2°, 67.0° and 69.1°
238 correspond to the (101), (002), (110), (112), (200), (103), (211) and (202) planes of tetragonal
239 In [PDF#85-1409], respectively. No diffraction peaks of In₂O₃ and In(OH)₃ were observed in
240 the XRD pattern. The sharp diffraction peaks imply a high crystallinity of *mp*-In, which agrees
241 with the HRTEM analysis. The full-scan XPS spectrum (**Figure 3b**) suggests that the obtained
242 *mp*-In catalyst is composed of In without other elements as impurities. For the In 3d XPS
243 spectrum (**Figure 3c**), the peaks at 443.7 and 451.3 eV correspond to In 3d_{5/2} and In 3d_{3/2},
244 respectively, suggesting the presence of the In (0) state. The characteristic peak pair of In (III)
245 was not detected [35]. This finding confirms that no oxidation species exist in the nanocatalyst,
246 which is consistent with the results of XRD analysis, and indicating that the obtained *mp*-In

247 catalyst is stable at ambient atmosphere.



248

249 **Figure 3.** (a) XRD patterns of the *mp*-In (black line) and the standard pure In (red line); (b) full
250 XPS spectrum of *mp*-In; (c) high-resolution XPS spectra of In 3d peaks; (d) nitrogen adsorption
251 isotherms of the *mp*-In (black) and commercial In (red) catalysts.

252 The textural properties of the prepared *mp*-In catalyst and commercial In particles were
253 compared using nitrogen gas adsorption (**Figure 3d**). A clear hysteresis loop is found in a wide
254 relative pressure range ($0.4 < P/P_0 < 0.9$) because of capillary condensation, which indicates
255 the existence of a large number of mesoporous structures in the *mp*-In catalyst. The
256 corresponding Brunauer-Emmett-Teller (BET) specific surface area of *mp*-In and commercial
257 In was calculated to be 504 and $66 \text{ m}^2 \text{ g}^{-1}$, respectively. The Barrett-Joyner-Halenda (BJH) pore
258 distribution reveals that the pores of the *mp*-In catalyst mainly center on $< 1.5 \text{ nm}$ and ~ 2.0

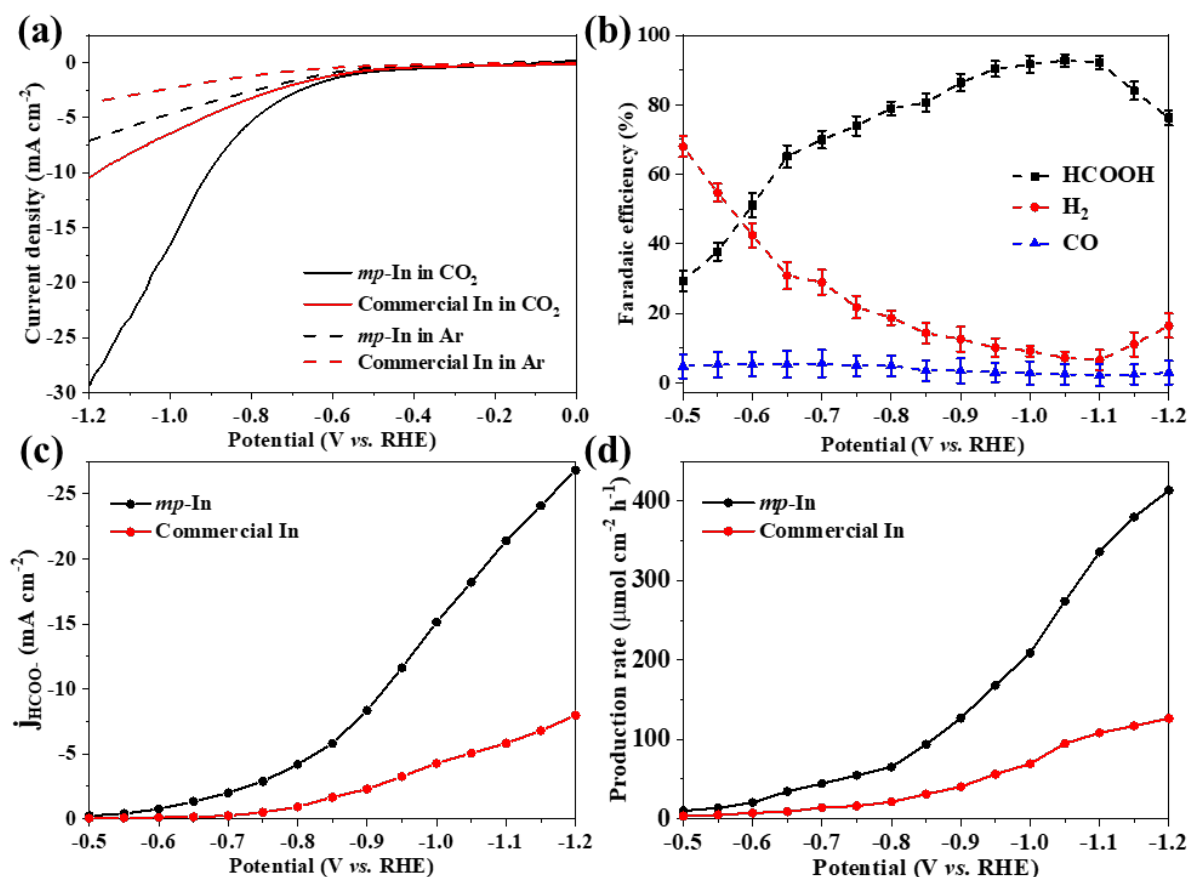
259 nm, while no clear porous structures are observed for the commercial In (**Figure S6**). The
260 formation of the mesoporous hierarchical structures is attributed to the hydrolysis of NaBH₄
261 generating hydrogen bubbles serving as geometric templates [36]. To verify this, a control
262 synthesis using a non-bubble reductant, sodium citrate, to replace the NaBH₄ has been
263 conducted. Under the same conditions, the *nano*-In catalyst synthesized with sodium citrate
264 has considerably less porous structures compared to the *mp*-In catalyst (TEM in **Figure S7**).
265 The *nano*-In catalyst shows the same hysteresis loop as the commercial In particles (**Figure**
266 **S8**). The specific surface area of the *nano*-In catalyst is 121 m² g⁻¹, considerably lower than
267 that of the *mp*-In catalyst. The reaction time is generally regarded as a key factor during
268 material synthesis and should be carefully controlled. In this study, if the reaction for the *mp*-
269 In catalyst preparation lasted too long (30 min), the In nanocrystals were found to aggregate
270 and form larger particles with reduced specific surface areas (**Figure S9a,b**). Additionally, due
271 to the lack of a protecting reducing atmosphere (H₂), the metal In in the center of particles were
272 oxidized, as evidenced by the EDS analysis (**Figure S9c-e**), which confirms the co-existence
273 of the In and O elements, with the In distributing uniformly over the nanoparticle, while the O
274 element was observed only in the center.

275

276 **3.2. Electrocatalytic performance of *mp*-In on CO₂RR to formate**

277 The electrocatalytic performance on CO₂RR using *mp*-In was investigated in a gas-tight
278 H-type electrochemical cell separated with a Nafion-117 membrane. The polarization curve in
279 CO₂-saturated 0.1 M KHCO₃ exhibits a cathodic current onset at around -0.7 V due to CO₂RR.
280 The current density continuously increases and reaches -29.4 mA cm⁻² at -1.2 V (**Figure 4a**).

281 Control experiments reveal that the HER is dominated in the cathode reaction when CO₂ is
 282 replaced with Ar. The current density diminishes markedly, which is in accordance with the
 283 relatively poor HER performance of the metal In. The current density of polarization curves
 284 for *mp*-In in CO₂- and Ar-saturated electrolytes (−29.4 mA cm^{−2} and −7.1 mA cm^{−2} at −1.2 V,
 285 respectively) are both considerably higher than that for the commercial In (−10.5 mA cm^{−2} and
 286 −3.7 mA cm^{−2} at −1.2 V, respectively). These results suggest that the electrocatalytic
 287 performance of the *mp*-In catalyst is significantly enhanced over the commercial In, which
 288 could be attributed to the mesoporous hierarchical structure of *mp*-In.



289
 290 **Figure 4.** Electrochemical measurements at different electrolytic potentials: (a) polarization
 291 curves in CO₂ or Ar-saturated 0.1 M KHCO₃; (b) faradaic efficiency of formate, H₂ and CO on
 292 the *mp*-In catalyst; (c) partial current density of formate; (d) formate production rate on the *mp*-

293 In and commercial In catalysts.

294 To analyze and quantify the reaction products, the electrochemical CO₂RR was performed
295 in a CO₂-saturated 0.1 M KHCO₃ solution for 1 hour. The various constant potentials were
296 chosen between -0.5 V and -1.2 V using the chronopotentiometry technique. Neither CH₄ nor
297 C₂H₄ were detected in the gaseous products. Formate is the primary CO₂RR product,
298 accompanied by trace amounts of CO and H₂. **Figure 4b** shows the effect of different potentials
299 on the FE of different products. At a potential of -0.5 V, the reproducible formate is firstly
300 detected reliably for *mp*-In with an FE of 29.3%, while the FE of H₂ is up to 67.9%. Increasing
301 the over-potential significantly enhances the FE of formate to > 90% at -0.95 V, reaching a
302 peak FE of 92% at -1.1 V, before gradually declining due to the diffusion-limitation of the
303 electrochemical reaction. By contrast, the FE of H₂ decreases rapidly and reaches a trough at -
304 1.1 V. In the CO₂RR process, the FE of CO remains at < 6%. These findings indicate that H₂ is
305 the dominant byproduct from the HER, which competes against the formation of formate in
306 the electrocatalytic CO₂RR, which is in agreement with the results from the prominent metal-
307 based electrocatalysts (e.g., Sn, Bi, In and Pb) [31,40-46]. To further confirm the superior
308 performance of *mp*-In on CO₂RR, the commercial In was again used as the CO₂RR
309 electrocatalyst under the same conditions. As shown in **Figure S10**, the formate is measured
310 reproducibly with an FE of 11.4% at -0.7 V and 69.7% at -1.05 V. A more negative potential
311 of CO₂RR indicates that the performance of commercial In is inferior to the *mp*-In catalyst in
312 the electrochemical reduction of CO₂.

313

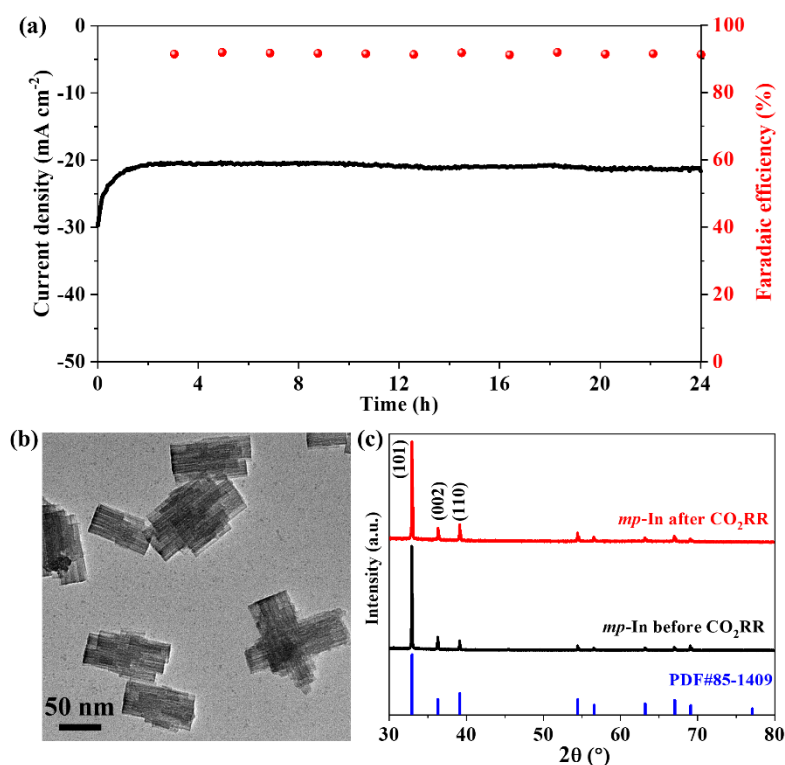
314

315 **Table 1.** Activity of different In-based catalysts in the electrocatalytic reduction of CO₂ to
 316 formate.

Electrocatalysts	Electrolyte	Formate FE _{max}	j _{HCOO⁻} at FE _{max} (mA cm ⁻²)	Ref.
<i>mp</i> -In	0.1 M KHCO ₃	90% @-0.95 V versus RHE	11.6	This work
<i>mp</i> -In	0.1 M KHCO ₃	92.6% @-1.1 V versus RHE	21.4	
H-InO _x nanoribbons	0.5 M NaHCO ₃	91.7% @-1.1 V versus RHE	15.2	[29]
In NPs	0.5 M K ₂ SO ₄	90% @-1.1 V versus RHE	NA	[31]
Anodized indium	0.5 M K ₂ SO ₄	87.2% @-1.7 V versus SCE	NA	[32]
Dendritic indium foams	0.5 M KHCO ₃	86% @-0.86 V versus RHE	5	[33]
Gas diffusion electrodes-In/C	0.1 M Na ₂ SO ₄	45% @-1.65 V versus Ag/AgCl	2.8	[34]
<i>hp</i> -In	0.1 M KHCO ₃	90% @-1.2 V versus RHE	67.5	[10]
Deposited In	0.5 M KHCO ₃	72.5% @-1.9 V versus Ag/AgCl	3	[47]
In ₂ O ₃ @C	0.5 M KHCO ₃	87.6% @-0.9 V versus RHE	14	[48]

317 Additionally, the partial current density of formate was estimated and plotted against the
 318 working potential for the *mp*-In and commercial In catalysts (**Figure 4c**). The *mp*-In catalyst
 319 shows a superior current density of j_{HCOO⁻} = 26.8 mA cm⁻¹ at -1.2 V, whereas that of the

320 commercial In is 7.9 mA cm^{-1} . **Figure 4d** shows that the formate production rate for the *mp*-In
 321 catalyst is $413.6 \text{ } \mu\text{mol cm}^{-2} \text{ h}^{-1}$ at -1.2 V , while this value is less than $126.4 \text{ } \mu\text{mol cm}^{-2} \text{ h}^{-1}$ for
 322 the commercial In sample. The large catalytic current density and high formate selectivity over
 323 a broad potential for the *mp*-In catalyst, are desirable with the advantages over other In-based
 324 CO_2RR electrocatalysts (**Table 1**).

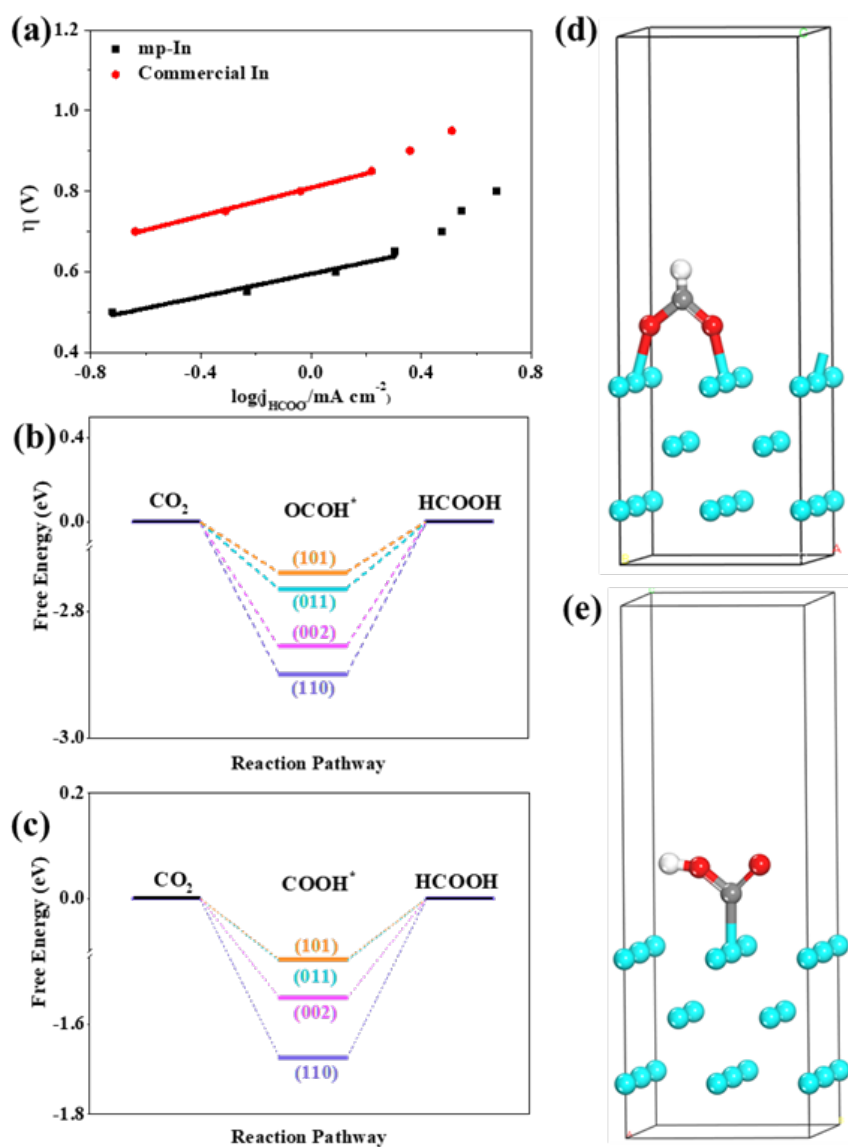


325
 326 **Figure 5.** (a) The long-term stability of the *mp*-In catalyst in the electrocatalytic CO_2 reduction
 327 to formate (a potential of -1.1 V for the test); (b) TEM image of *mp*-In; (c) XRD patterns of
 328 *mp*-In before and after the 24 h reaction.

329 The electrochemical stability of the *mp*-In and commercial In catalysts has been
 330 investigated under the optimal conditions in CO_2 -saturated 0.1 M KHCO_3 at a constant flow
 331 rate of 20 mL min^{-1} during long-term operation. The *mp*-In catalyst demonstrates outstanding
 332 electrochemical durability with a negligible performance decay after the 24 h continuous

333 electrolysis at -1.1 V (**Figure 5a**). The current density is maintained at around 20 mA cm⁻²
334 with the FE of formate being over 90% during the test. In addition, no significant changes in
335 the morphology of the spent *mp*-In nanocatalyst were observed, based on the TEM image
336 (**Figure 5b**). The XRD pattern (**Figure 5c**) and XPS spectrum (**Figure S11**) of the spent *mp*-In
337 nanocatalyst also remained almost unchanged, demonstrating the excellent durability of the
338 *mp*-In catalyst. These results prove that the *mp*-In is a potential electrocatalyst for CO₂
339 reduction to formate owing to its excellent catalytic activity, selectivity and durability.

340 Tafel plots were obtained at regions of low current density to understand the mechanism
341 of CO₂ reduction for the *mp*-In catalyst (**Figure 6a**), where the reaction is mainly limited by
342 electro-kinetics. The slope for the commercial In is 181 mV dec⁻¹, while the *mp*-In catalyst
343 exhibits a lower slope of 124 mV dec⁻¹, close to that (118 mV dec⁻¹) reported in previous studies
344 [49,50]. This result reveals that the reaction kinetics of the CO₂RR is limited by the initial one-
345 electron transfer to form an adsorbed CO₂* intermediate on the *mp*-In catalyst. The increase in
346 the Tafel slope at high current densities demonstrates a mass transport limitation for CO₂
347 reduction in this region due to the low CO₂ concentration in the electrolyte. It is generally
348 believed that the first electron transferred from the electrode to the CO₂* for the formation of
349 CO₂* is the rate-determining step of the CO₂RR [11, 51-54]. The faster initial electron transfer
350 for the CO₂ molecules on the *mp*-In surface than that on the commercial In surface suggests an
351 improved performance of the *mp*-In for CO₂RR. The bonding between the CO₂* and the
352 catalyst will further affect the generation of the next intermediates (OCHO* or COOH*) when
353 being protonated, and finally determining the product selectivity [11].



354

355 **Figure 6.** (a) The potential-dependent HCOO^- partial current density on the *mp*-In and
 356 commercial In catalysts; the free energy diagrams for (b) OCO^*H and (c) COOH^* on *mp*-In
 357 (110), (002), (011) and (101) planes, and optimized geometric structure of (d) OCO^*H and (e)
 358 COOH^* adsorbed on In (110), in which In, C, O and H atoms are represented by azure, gray,
 359 red and white spheres, individually.

360

361 3.3. Origin of the improved CO_2RR activity and selectivity over *mp*-In

362 To gain further insights into the mechanism in the electrocatalytic CO_2 reduction to

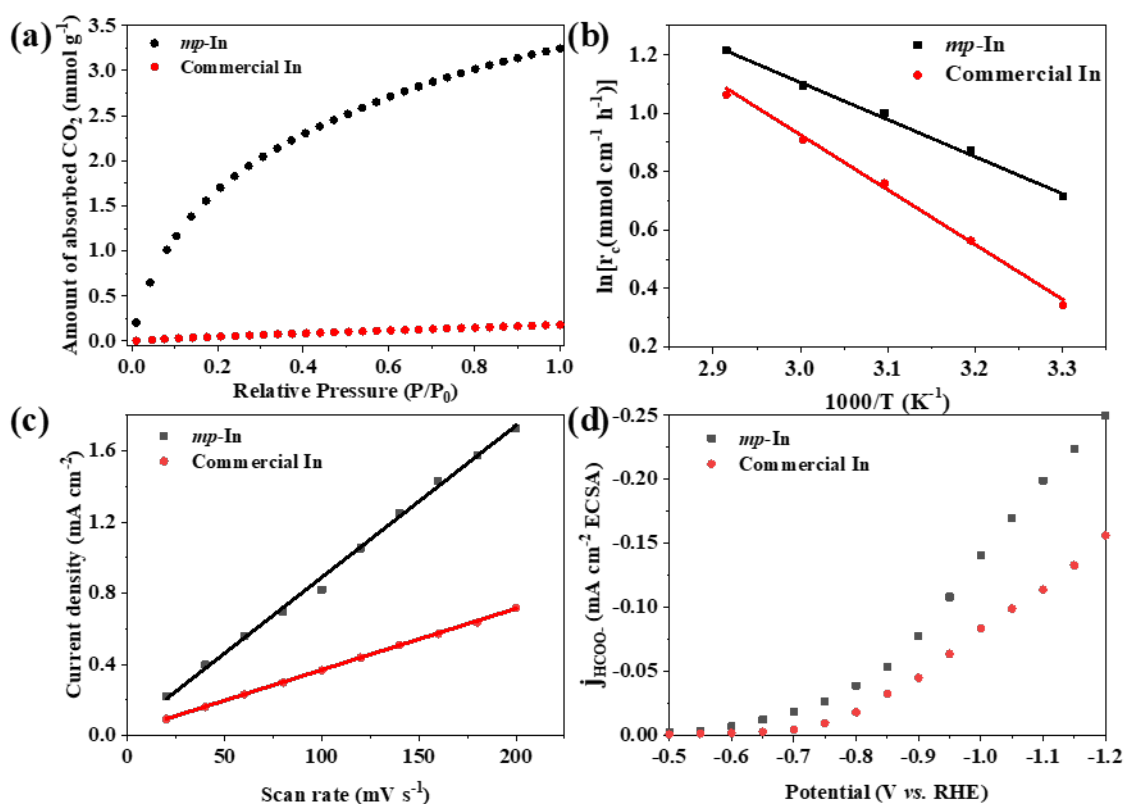
363 formate and the origin of the enhanced activity of *mp*-In, DFT calculations were carried out to
364 simulate the CO₂RR on In (110), (002), (011) and (101) planes considering possible reaction
365 pathways under the operating conditions. The free energy focuses on the formation of OCHO*
366 and COOH*, both of which are the important intermediates in the CO₂RR [10,34,35]. The four
367 surface planes favor the formation of OCHO* (in **Figure 6b** and **Table S1**) over COOH* (in
368 **Figure 6c** and **Table S2**), with the optimized geometric structures of these two intermediates
369 adsorbed on the surfaces of the *mp*-In (110) (**Figure 6d** and **6e**). In particular, the (110) plane
370 is able to stabilize the OCHO* and therefore is the most active for formate production, which
371 is the main crystal plane for *mp*-In confirmed by the HRTME images of *mp*-In (**Figure 2c** and
372 **2d**). This generally contributes to the observed high activity and Faradaic efficiency for formate
373 on the *mp*-In catalyst.

374 The remarkable enhancement in the performances (activity, selectivity and stability) in
375 the CO₂RR over the *mp*-In catalyst may be ascribed to its structural features. Firstly, the
376 mesoporous structure of *mp*-In contains more edge and low coordinate sites, which have been
377 proven to enhance the production of intermediates, and to promote the CO₂RR, as confirmed
378 by previous studies [53, 55]. Furthermore, the advanced structure of *mp*-In enhances the
379 adsorption of CO₂, which is conducive to lower potential and higher FEs in the CO₂RR. The
380 volumetric CO₂ absorption measurement, carried out to explore the reason for the enhanced
381 CO₂RR activity in this work, discloses that *mp*-In adsorbs more CO₂ than the commercial In.
382 The amount of adsorbed CO₂ was 3.25 mmol g⁻¹ for *mp*-In and only 0.18 mmol g⁻¹ for the
383 commercial In (**Figure 7a**). Compared to the commercial In catalyst, *mp*-In exhibits a
384 significantly enhanced CO₂ adsorption capacity, which can be evidenced by a much stronger

385 absorption at 2350 cm^{-1} in the DRIFTS spectra (**Figure S12**). Secondly, the higher density of
386 the exposed sites in the mesoporous structure of *mp*-In can lower the activation energy (E_a) of
387 the CO_2RR , which resulted in achieving better performance in many reactions. The reactive
388 sites at the edges of the nanocatalysts possess unsaturated coordination sites as well as dangling
389 bonds, which decrease the activation energy barrier and enable the stabilization of the reaction
390 intermediates, as suggested in the literature [53, 55, 56]. If the catalysts are active for the
391 CO_2RR , they will provide a path with a lower activation energy compared to the uncatalyzed
392 reactions, thus increasing the reaction rate constant. The reaction rate of CO_2RR is defined as
393 the formate production rate in the electrolysis reaction at different temperatures. The estimated
394 apparent E_a of the CO_2RR is 15.3 kJ mol^{-1} and 22.6 kJ mol^{-1} in electrolytes for the *mp*-In and
395 the commercial In catalysts, respectively (**Figure 7b**).

396 Additionally, the mesoporous structures are evenly dispersed over the surface of the *mp*-
397 In catalyst composed of nanobelts, which enrich the electrocatalysts with the formation of
398 active sites. To estimate the catalytic properties with the surface structures, cyclic
399 voltammograms (CVs) at different scanning rates were recorded for the *mp*-In and commercial
400 In catalysts in 0.1 M KHCO_3 (**Figure S13**). The electrochemical surface areas of the In
401 catalysts were determined by measuring the double-layer capacitance. As shown in **Figure 7c**,
402 the double-layer capacitance (C_{dl}) of *mp*-In is 4.3 mF , 2.5 times larger than that of the
403 commercial In catalyst (1.7 mF), suggesting that the *mp*-In catalyst has more active sites for
404 CO_2RR . Based on the obtained C_{dl} values, the ECSA of the *mp*-In was calculated to be 107.5
405 cm^{-2} , much higher than that of the commercial In (42.5 cm^{-2}). **Figure. 7d** shows the specific
406 current densities for formate production (normalized to specific ESCA values) during the

407 CO₂RR. The *mp*-In catalyst exhibits higher specific formate current densities ($j_{\text{HCOO}^-}/\text{ECSA}$) at
 408 all testing potentials (-0.5 to -1.2 V) compared with the commercial In, further confirming its
 409 superior catalytic performance for electrocatalytic CO₂-to-formate conversion. The
 410 mesoporous hierarchical structure of the *mp*-In catalyst could significantly decrease the
 411 apparent E_a and efficiently promote the CO₂RR.



412
 413 **Figure 7.** (a) The CO₂ adsorption isotherms and (b) apparent activation energy (E_a) for CO₂RR;
 414 (c) current density at different scan rates; (d) specific current density for formate production at
 415 different potentials.

416 4. Conclusion

417 This paper reports a mesoporous In (*mp*-In) electrocatalyst synthesized using a green and
 418 facile solution method for the highly selective and active electroreduction of CO₂ to formate.
 419 Remarkably, a formate selectivity of over 90% (Faradaic efficiency) with a high current density

420 of over -29.4 mA cm^{-2} was achieved over a potential from -0.95 V to -1.1 V . The *mp*-In catalyst
421 also exhibited outstanding stability in the 24 h reaction without a visible catalyst deactivation.
422 DFT calculations further reveal the plane-dependent catalytic activity and conclude that the
423 plane surfaces (110) and (002) of the *mp*-In catalyst contribute to the stabilization of *OCHO,
424 a key intermediate for formate generation. This active, durable and selective electrocatalyst has
425 great potential to enhance the technological and economic viability of CO₂-to-formate
426 conversion. Moreover, this work also demonstrates that developing novel nanostructure
427 catalysts, with larger surface areas, abundant active surface sites and edge/low-coordinated
428 sites is critical to enhance the efficiency of electrocatalytic CO₂RR, which may provide
429 important insights into the facile fabrication of porous hierarchical nanostructures for selective
430 CO₂RR.

431

432 **Appendix A. Supplementary data**

433 Supplementary data to this article can be found online.

434

435 **Declaration of Competing Interest**

436 The authors declare that they have no known competing financial interests or personal
437 relationships that could have appeared to influence the work reported in this paper.

438

439

440

441

442 **Acknowledgements**

443 This project has received funding from the European Union's Horizon 2020 research and
444 innovation programme under the Marie Skłodowska-Curie grant agreement No 823745.

445

446 **References**

- 447 [1] J. Wang, S. Kattel, C. J. Hawxhurst, J. H. Lee, B. M. Tackett, K. Chang, N. Rui, C. J. Liu,
448 J. G. Chen. Enhancing activity and reducing cost for electrochemical reduction of CO₂ by
449 supporting palladium on metal carbides. *Angew. Chem. Int. Ed.* 58 (2019) 6271-6275.
- 450 [2] Z. Zhu, X. Liu, C. Bao, K. Zhang, C. Song, Y. Xuan. How efficient could photocatalytic
451 CO₂ reduction with H₂O into solar fuels be? *Energy Convers. Manag.* 222 (2020) 113236.
- 452 [3] S.L. Zhao, D.W. Wang, R. Amal, L. Dai, Carbon-based metal-free catalysts for key
453 reactions involved in energy conversion and storage. *Adv. Mater.* 31 (2019) 1801526.
- 454 [4] R. Zhou, R. Zhou, Y. Xian, Z. Fang, X. Lu, K. Bazaka, A. Bogaerts, K. K. Ostrikov,
455 Plasma-enabled catalyst-free conversion of ethanol to hydrogen gas and carbon dots near
456 room temperature. *Chem. Eng. J.* 382 (2020) 122745.
- 457 [5] C. G. Morales-Guio, E. R. Cave, S. A. Nitopi, J. T. Feaster, L. Wang, K. P. Kuhl, A.
458 Jackson, N. C. Johnson, D. N. Abram, T. Hatsukade, C. Hahn, T. F. Jaramillo, Improved CO₂
459 reduction activity towards C₂+ alcohols on a tandem gold on copper electrocatalyst. *Nat.*
460 *Catal.* 1 (2018) 764-771.
- 461 [6] A. George, B. Shen, M. Craven, Y. Wang, D. Kang, C. Wu, X. Tu, A review of non-thermal
462 plasma technology: a novel solution for CO₂ conversion and utilization, *Renew. Sust. Energy*
463 *Rev.* 135 (2021) 109702.

464 [7] J. Zhang, M. Ren, X. Li, Q. Hao, H. Chen, X. Ma. Ni-based catalysts prepared for CO₂
465 reforming and decomposition of methane. *Energy Convers. Manag.* 205 (2020) 112419.

466 [8] T. N. Do, J. Kim, Green C₂-C₄ hydrocarbon production through direct CO₂ hydrogenation
467 with renewable hydrogen: Process development and techno-economic analysis. *Energy*
468 *Convers. Manage.* 214 (2020) 112866.

469 [9] S. Li, L. Yang, O. Ola, M. Maroto-Valer, X. Du, Y. Yang, Photocatalytic reduction of CO₂
470 by CO co-feed combined with photocatalytic water splitting in a novel twin reactor. *Energy*
471 *Convers. Manag.* 116 (2016) 184-193.

472 [10] W. Luo, W. Xie, M. Li, J. Zhang, A. Zuttel, 3D hierarchical porous indium catalyst for
473 highly efficient electroreduction of CO₂. *J. Mater. Chem. A* 7 (2019) 4505-4515.

474 [11] N. Han, P. Ding, L. He, Y. Y. Li, Y.G. Li, Promises of Main Group Metal-Based
475 Nanostructured Materials for Electrochemical CO₂ Reduction to Formate. *Adv. Energy Mater.*
476 10 (2020) 1902338.

477 [12] J. H. Koh, D. H. Won, T. Eom, N. K. Kim, K. D. Jung, H. Kim, Y. J. Hwang, B. K. Min,
478 Facile CO₂ electro-reduction to formate via oxygen bidentate intermediate stabilized by high-
479 index planes of Bi dendrite catalyst. *ACS Catal.* 7 (2017) 5071-5077.

480 [13] K. P. Kuhl, T. Hatsukade, E. R. Cave, D. N. Abram, J. Kibsgaard, T. F. Jaramillo,
481 Electrocatalytic conversion of carbon dioxide to methane and methanol on transition metal
482 surfaces. *J. Am. Chem. Soc.* 136 (2014) 14107-14113.

483 [14] C. Kim, H. S. Jeon, T. Eom, M. S. Jee, H. Kim, C. M. Friend, B. K. Min, Y. J. Hwang,
484 Achieving selective and efficient electrocatalytic activity for CO₂ reduction using
485 immobilized silver nanoparticles. *J. Am. Chem. Soc.* 137 (2015) 13844-13850.

486 [15] R. Reske, H. Mistry, F. Beharid, B. Roldan Cuenya, P. Strasser, Particle size effects in
487 the catalytic electroreduction of CO₂ on Cu nanoparticles. *J. Am. Chem. Soc.* 136 (2014)
488 6978-6986.

489 [16] F. S. Roberts, K.P. Kuhl, A. Nilsson, High selectivity for ethylene from carbon dioxide
490 reduction over copper nanocube electrocatalysts. *Angew. Chem. Int. Ed.* 54 (2015) 5179-
491 5182.

492 [17] J. F. Xie, J. J. Chen, Y. X. Huang, X. Zhang, W. K. Wang, G. X. Huang, H. Q. Yu,
493 Selective electrochemical CO₂ reduction on Cu-Pd heterostructure. *Appl. Catal. B: Environ.*
494 270 (2019) 118864.

495 [18] M. F. Baruch, J. E. Pander, J. L. White, A. B. Bocarsly, Mechanistic insights into the
496 reduction of CO₂ on tin electrodes using in situ ATR-IR spectroscopy. *ACS Catal.* 5 (2015)
497 3148-3156.

498 [19] S. Zhang, P. Kang, T. J. Meyer, Nanostructured tin catalysts for selective electrochemical
499 reduction of carbon dioxide to formate. *J. Am. Chem. Soc.* 136 (2014) 1734-1737.

500 [20] N. Han, Y. Wang, H. Yang, J. Deng, J.H. Wu, Y.F. Li, Y.G. Li, Ultrathin bismuth
501 nanosheets from in situ topotactic transformation for selective electrocatalytic CO₂ reduction
502 to formate. *Nat. Commun.* 9 (2018) 1320.

503 [21] S.L. Zhao, S. Li, T. Guo, S. S. Zhang, J. Wang, Y.P. Wu, Y.H. Chen, Advances in Sn-
504 based catalysts for electrochemical CO₂ reduction. *Nano-Micro. Lett.* 11 (2019) 62.

505 [22] Y. Hori, K. Kikuchi, S. Suzuki, Production of Co and CH₄ in electrochemical reduction
506 of CO₂ at metal-electrodes in aqueous hydrogencarbonate solution, *Chem. Lett.* 11 (1985)
507 1695-1698.

- 508 [23] Y. Hori, H. Wakebe, T. Tsukamoto, O. Koga, Electrocatalytic process of Co selectivity in
509 electrochemical reduction of CO₂ at metal-electrodes in aqueous-media. *Electrochim. Acta* 39
510 (1994) 1833-1839.
- 511 [24] M. Tahir, B. Tahir, N. A. S. Amin, A. Muhammad , Photocatalytic CO₂ methanation over
512 NiO/In₂O₃ promoted TiO₂ nanocatalysts using H₂O and/or H₂ reductants. *Energy Convers.*
513 *Manage.* 119 (2016) 368-378.
- 514 [25] Y. H. Chen, M.W. Kanan, Tin oxide dependence of the CO₂ reduction efficiency on tin
515 electrodes and enhanced activity for tin/tin oxide thin-film catalysts. *J. Am. Chem. Soc.* 134
516 (2012) 1986-1989.
- 517 [26] F. C. Lei, W. Liu, Y. F. Sun, J. Q. Xu, K. T. Liu, L. Liang, T. Yao, B. C. Pan, S. Q. Wei,
518 Y. Xie, Metallic tin quantum sheets confined in graphene toward high-efficiency carbon
519 dioxide electroreduction, *Nat. Commun.* 7 (2016) 12697.
- 520 [27] Y. Y. Cheng, P. F. Hou, H. Pan, H. Shi, P. Kang, Selective electrocatalytic reduction of
521 carbon dioxide to oxalate by lead tin oxides with low overpotential. *Appl. Catal. B: Environ.*
522 272 (2020) 118954.
- 523 [28] W. C. Ma, S. J. Xie, X. G. Zhang, F. F. Sun, J. C. Kang, Z. Jiang, Q. H. Zhang, D. Y. Wu,
524 Y. Wang, Promoting electrocatalytic CO₂ reduction to formate via sulfur-boosting water
525 activation on indium surfaces. *Nat. Commun.* 10 (2019) 892.
- 526 [29] J. B. Zhang, R. G. Yin, Q. Shao, T. Zhu, X. Q. Huang, Oxygen vacancies in amorphous
527 InOx nanoribbons enhance CO₂ adsorption and activation for CO₂ electroreduction. *Angew.*
528 *Chem. Int. Ed.* 58 (2019) 5609-5613.
- 529 [30] Z. B. Hoffman, T. S. Gray, K. B. Moraveck, T. B. Gunnoe, G. Zangari, Electrochemical

530 reduction of carbon dioxide to syngas and formate at dendritic copper-indium
531 electrocatalysts. *ACS Catal.* 7 (2017) 5381-5390.

532 [31] J. L. White, A. B. Bocarsly, Enhanced carbon dioxide reduction activity on indium-based
533 nanoparticles. *J. Electrochem. Soc.* 163 (2016) 410-416.

534 [32] Z. M. Detweiler, J. L. White, S. L. Bernasek, A. B. Bocarsly, Anodized Indium Metal
535 Electrodes for Enhanced Carbon Dioxide Reduction in Aqueous Electrolyte. *Langmuir* 30
536 (2014) 7593-7600.

537 [33] Z. Xia, M. Freeman, D. X. Zhang, B. Yang, L. C. Lei, Z. J. Li, Y. Hou, Highly selective
538 electrochemical conversion of CO₂ to HCOOH on dendritic indium Foams.
539 *Chemelectrochem* 5 (2018) 253-259.

540 [34] Z. Bitar, A. Fecant, E. Trela-Baudot, S. Chardon-Noblat, D. Pasquier, Electrocatalytic
541 reduction of carbon dioxide on indium coated gas diffusion electrodes-Comparison with
542 indium foil. *Appl. Catal. B: Environ.* 189 (2016) 172-180.

543 [35] S. Rasul, D. H. Anjum, A. Jedidi, Y. Minenkov, L. Cavallo, K. Takanebe, A highly
544 selective copper-indium bimetallic electrocatalyst for the electrochemical reduction of
545 aqueous CO₂ to CO. *Angew. Chem. Int. Ed.* 54 (2015) 2146-2150.

546 [36] H.C. Shin, J. Dong, M. L. Liu, Nanoporous structures prepared by an electrochemical
547 deposition process. *Adv. Mater.* 15 (2003) 1610-1614.

548 [37] H. Yang, N. Han, J. Deng, J. H. Wu, Y. Wang, Y. P. Hu, P. Ding, Y. F. Li, Y. G. Li, J. Lu,
549 Selective CO₂ reduction on 2D mesoporous Bi nanosheets. *Adv. Energy Mater.* 8 (2018)
550 1801536.

551 [38] H. Deng, C. Zhang, Y. C. Xie, T. Tumlin, L. Giri, S. P. Karna, J. Lin, Laser induced

552 MoS₂/carbon hybrids for hydrogen evolution reaction catalysts. *J. Mater. Chem. A* 4 (2016)
553 6824-6830.

554 [39] S. B. Liu, X. F. Lu, J. Xiao, X. Wang, X. W. Lou, Bi₂O₃ nanosheets grown on multi-
555 channel carbon matrix to catalyze efficient CO₂ electroreduction to HCOOH. *Angew. Chem.*
556 *Int. Ed.* 58 (2019) 13828-13833.

557 [40] N. Han, P. Ding, L. He, Y. Y. Li, Y. G. Li, Promises of main group metal-based
558 nanostructured materials for electrochemical CO₂ reduction to formate. *Adv. Energy Mater.*
559 10 (2020) 1902338.

560 [41] X. L. Zhang, X.H. Sun, S. X. Guo, A. M. Bond, J. Zhang, Formation of lattice-dislocated
561 bismuth nanowires on copper foam for enhanced electrocatalytic CO₂ reduction at low
562 overpotential. *Energ. Environ. Sci.* 12 (2019) 1334-1340.

563 [42] C.L. Liang, B. Kim, S.Z. Yang, Y. Liu, C.F. Woellner, Z.Y. Li, R. Vajtai, W. Yang, J.J.
564 Wu, P.J.A. Kenis, P.M. Ajayan, High efficiency electrochemical reduction of CO₂ beyond the
565 two-electron transfer pathway on grain boundary rich ultra-small SnO₂ nanoparticles. *J.*
566 *Mater. Chem. A* 6 (2018) 10313-10319.

567 [43] Y. Zhao, J.J. Liang, C.Y. Wang, J.M. Ma, G.G. Wallace, Tunable and efficient tin
568 modified nitrogen-doped carbon nanofibers for electrochemical reduction of aqueous carbon
569 dioxide. *Adv. Energy Mater.* 8 (2018) 1702524.

570 [44] Y. Zhang, X. L. Zhang, Y. Z. Ling, F. W. Li, A. M. Bond, J. Zhang, Controllable
571 synthesis of few-layer bismuth subcarbonate by electrochemical exfoliation for enhanced
572 CO₂ reduction performance. *Angew. Chem. Int. Ed.* 57 (2018) 13283-13287.

573 [45] Q. F. Gong, P. Ding, M. Q. Xu, X. R. Zhu, M. Y. Wang, J. Deng, Q. Ma, N. Han, Y. Zhu,

574 J. Lu, Z. X. Feng, Y. F. Li, W. Zhou, Y. G. Li, Structural defects on converted bismuth oxide
575 nanotubes enable highly active electrocatalysis of carbon dioxide reduction. *Nat. Commun.*
576 10 (2019) 2807.

577 [46] Y. Kwon, J. Lee, Formic acid from carbon dioxide on nanolayered electrocatalyst.
578 *Electrocatalysis* 1 (2010) 108-115.

579 [47] B. Bohlen, D. Wastl, J. Radomski, V. Sieber and L. Vieira, electrochemical CO₂
580 reduction to formate on indium catalysts prepared by electrodeposition in deep eutectic
581 solvents. *Electrochem. Commun.* 110 (2020) 106597.

582 [48] K. W. Mou, Z. P. Chen, S. Y. Yao and L. C. Liu, Enhanced electrochemical reduction of
583 carbon dioxide to formate with in-situ grown indium-based catalysts in an aqueous
584 electrolyte. *Electrochim. Acta* 289 (2018) 65-71.

585 [49] Z. P. Chen, K. W. Mou, X. H. Wang, L. C. Liu, Nitrogen-doped graphene quantum dots
586 enhance the activity of Bi₂O₃ nanosheets for electrochemical reduction of CO₂ in a wide
587 negative potential region. *Angew. Chem. Int. Ed.* 57 (2018) 12790-12794.

588 [50] C.W. Lee, N. H. Cho, K. D. Yang, K. T. Nam, Reaction mechanisms of the
589 electrochemical conversion of carbon dioxide to formic acid on tin oxide electrodes.
590 *Chemelectrochem* 4 (2017) 2130-2136.

591 [51] R. Nazir, A. Kumar, M.A.S. Saad, S. Ali, Development of CuAg/Cu₂O nanoparticles on
592 carbon nitride surface for methanol oxidation and selective conversion of carbon dioxide into
593 formate. *J. Colloid Interf. Sci.* 578 (2020) 726-737.

594 [52] R. Nazir, A. Kumar, M.A.S. Saad, A. Ashok, Synthesis of hydroxide nanoparticles of
595 Co/Cu on carbon nitride surface via galvanic exchange method for electrocatalytic CO₂

596 reduction into formate. *Colloids and Surfaces A* 598 (2020) 124835.

597 [53] R. Nazir, A. Khalfani, O. Abdelfattah, A. Kumar, M.A.S. Saad, S. Ali, *Nanosheet*

598 *Synthesis of Mixed Co₃O₄/CuO via Combustion Method for Methanol Oxidation and Carbon*

599 *Dioxide Reduction. Langmuir* 36 (2020) 12760-12771.

600 [54] R. Nazir, A. Kumar, S. Ali, M.A.S. Saad, M.J. Al-Marri, *Galvanic Exchange as a Novel*

601 *Method for Carbon Nitride Supported CoAg Catalyst Synthesis for Oxygen Reduction and*

602 *Carbon Dioxide Conversion. Catalysts* 9 (2019) 860.

603 [55] Q. Shen, X. F. Huang, J. B. Liu, C. Y. Guo, G. H. Zhao, *Biomimetic*

604 *photoelectrocatalytic conversion of greenhouse gas carbon dioxide: Two-electron reduction*

605 *for efficient formate production. Appl. Catal. B: Environ.* 201 (2017) 70-76.

606 [56] Z. Y. Sun, N. T. Talreja, H. C. Tao, J. Texter, M. Muhler, J. Strunk, J. F. Chen, *Catalysis*

607 *of Carbon Dioxide Photoreduction on Nanosheets: Fundamentals and Challenges. Angew.*

608 *Chem. Int. Ed.* 57 (2018) 7610-7627.